



## Holographic Generation of Highly Twisted Electron Beams

Vincenzo Grillo,<sup>1,2</sup> Gian Carlo Gazzadi,<sup>1</sup> Erfan Mafakheri,<sup>1,3</sup> Stefano Frabboni,<sup>1,3</sup>  
Ebrahim Karimi,<sup>4,\*</sup> and Robert W. Boyd<sup>4,5</sup>

<sup>1</sup>CNR-Istituto Nanoscienze, Centro S3, Via G. Campi 213/a, I-41125 Modena, Italy

<sup>2</sup>CNR-IMEM Parco Area delle Scienze 37/A, I-43124 Parma, Italy

<sup>3</sup>Dipartimento FIM, Università di Modena e Reggio Emilia, Via G. Campi 213/a, I-41125 Modena, Italy

<sup>4</sup>Department of Physics, University of Ottawa, 25 Templeton, Ottawa, Ontario, K1N 6N5 Canada

<sup>5</sup>Institute of Optics, University of Rochester, Rochester, New York 14627, USA

(Received 1 September 2014; published 23 January 2015)

Free electrons can possess an intrinsic orbital angular momentum, similar to those in an electron cloud, upon free-space propagation. The wave front corresponding to the electron's wave function forms a helical structure with a number of twists given by the *angular speed*. Beams with a high number of twists are of particular interest because they carry a high magnetic moment about the propagation axis. Among several different techniques, electron holography seems to be a promising approach to shape a *conventional* electron beam into a helical form with large values of angular momentum. Here, we propose and manufacture a nanofabricated phase hologram for generating a beam of this kind with an orbital angular momentum up to  $200\hbar$ . Based on a novel technique the value of orbital angular momentum of the generated beam is measured and then compared with simulations. Our work, apart from the technological achievements, may lead to a way of generating electron beams with a high quanta of magnetic moment along the propagation direction and, thus, may be used in the study of the magnetic properties of materials and for manipulating nanoparticles.

DOI: 10.1103/PhysRevLett.114.034801

PACS numbers: 41.85.Ct, 42.50.Tx

Almost a century ago, Rutherford and Bohr proposed a model, the so-called *Bohr model*, to describe the structure of atoms in which model atoms consist of a positive nucleus surrounded by orbiting electrons [1,2]. Even in this semi-classical model, orbiting electrons possess a quantized orbital motion, i.e., orbital angular momentum (OAM). This quantization, indeed, lies at the heart of the rotationally symmetric nature of the atom. However, it took quite a long time to theoretically predict and experimentally demonstrate that free electrons can also carry a quantized OAM value upon free-space propagation [3–5]. The wave front of electrons carrying a quantized OAM forms a helical shape  $\exp(im\varphi)$  with an integer winding index  $m$ , where  $\varphi$  is the azimuthal angle in polar coordinates. A free electron with such a helical phase front possesses an OAM value of  $m\hbar$  along the propagation direction and has a magnetic moment  $\mu_{\text{OAM}} = m\mu_B$  oriented along the beam axis with a polarity that depends on the sign of  $m$ .  $\mu_B = e\hbar/(2m_e)$  is the Bohr magneton of the electron,  $\hbar$  is the Planck constant, and  $e$  and  $m_e$  are the electron charge and rest mass, respectively. This magnetic moment, unlike the spin Bohr magneton, in principle is unbounded and can be large if desired. Nonetheless, it is bounded by the accuracy of phase modulation and the numerical aperture of the electron optics [6]. The spatial density distribution of these electrons in the transverse plane—orthogonal to the propagation direction—appears to be a doughnut shape, because a helical phase is undefined at the origin. Moreover, the

current density associated with the wave function of “twisted” electrons circulates about the origin; thus, these beams are also called electron vortex beams (EVBs). Twisted electron beams (EBs) possess a novel *magnetic moment*  $\mu_{\text{OAM}}$  along the propagation axis and, thus, found immediate applications in the study of materials [7,8]. Among those applications, manipulating nanoparticles [9] and measuring magnetic dichroism [10] are primary examples. In the latter case, the magnetic moment of EVBs, in addition to spin  $\frac{1}{2}$  of the electron, is coupled into the internal dynamics of atoms [11]. Several different methods analogous to optical counterparts such as spiral-phase plates [4], fork holograms [5,6,12], astigmatic mode converters [13], spin to OAM [14,15], and tuning of a multipolar aberration corrector [16,17] have been proposed to generate twisted electrons, and some have been experimentally verified.

In this Letter, we report the generation of twisted EBs with an OAM value of  $200\hbar$ —the highest electron OAM quanta up to now. Achieving an EB with a high number of twists provides the possibility of exploring the transition between the quantum and classical regimes of electromagnetic radiation inside a medium, where the spin-induced effects are diminished [18]. This transition is particularly interesting in view of observing phenomena such as polarization radiation, which has never been experimentally observed. The generated beam is manipulated by a nanofabricated phase hologram with  $200\ 2\pi$ -phase variations around the origin. Such a high phase variation around

the origin is beyond the hologram's spatial-fringe resolution. Thus, we examine the OAM purity of the generated beam for two different cases, where the center of the hologram is excluded or included. The results reveal that the generated beam carries a specific *OAM spectrum* determined by the resolution of phase modulation of the hologram. Thus, for this special case the region beyond the hologram's spatial resolution must be excluded. Finally, we analyze the radial distribution of the generated beam that is relevant to study electron-magnetic interactions [19].

Let us now briefly discuss the holographic approach of generating an EB with a helical phase front of  $\langle \mathbf{r} | \psi_m \rangle = \exp(im\varphi)$ . Such a beam can be generated in different ways: (i) a pure phase object (spiral phase plate) with linear phase scaling, (ii) an amplitude mask with a dislocation at the center, and (iii) a pure phase mask (PM) with limited phase mapping in the interval of  $[a, b]$ , where  $a, b \in \{-\pi, \dots, \pi\}$  (examples are reported in Refs. [20–22]). The latter case gives a more realistic way to generate an EB with a desired shape, since a carrier can be used to “sift” the desired beam from the reference beam. The shape of the PM used to generate a twisted EB is identical to the amplitude mask but entirely transparent to the electrons. Thus, almost all electrons travel through the mask without being absorbed. Nonetheless, electron-electron elastic scattering introduced by the mask changes the phase of the electron wave packet in the transverse plane. This phase alteration is proportional to the mean inner potential of the material,  $V_{\text{mip}}$  [23]. A PM with a thickness of  $t(x, y)$  varying in the transverse  $x - y$  plane introduces a coordinate-dependent phase change of  $\Delta\chi(x, y)$ , given by

$$\Delta\chi = \frac{2\pi e}{\lambda} \frac{\mathcal{E} + \mathcal{E}_0}{\mathcal{E}(\mathcal{E} + 2\mathcal{E}_0)} V_{\text{mip}} t(x, y), \quad (1)$$

where  $\lambda$  is the de Broglie wavelength of the electron and  $\mathcal{E}$  and  $\mathcal{E}_0$  are the kinetic and the rest energy of the electrons, respectively [24]. The thickness function  $t(x, y)$  determines the induced phase alteration and, consequently, the efficiency of the generated beam.

In this work, we focus on generating an EB with a high number of twists. Thus, at a cost of efficiency, a PM with a sinusoidal modulation is used to generate EBs, because it provides better control on the mask structure. Therefore, we implement a sinusoidal modulation, i.e.,  $t(x, y) = t_0[1 + \cos(m\varphi + 2\pi x/\Lambda)]/2$ , where  $t_0$  is the modulation depth,  $\Lambda$  is the grating period, and  $\varphi = \arctan(y/x)$  with  $x$  and  $y$  being Cartesian coordinates (see Supplemental Material for more details [25]). The structure of the PM and the scanning electron microscope (SEM) image of the fabricated hologram are shown in Figs. 1(a) and 1(b), respectively [fine structure of the nanofabricated computer generated holograms (CGHs) is shown in Supplemental Material [25]]. The nanofabricated CGH, shown in Fig. 1(b), is generated with the same approach reported in Refs. [12,21], where a Ga-ion focused ion beam is used

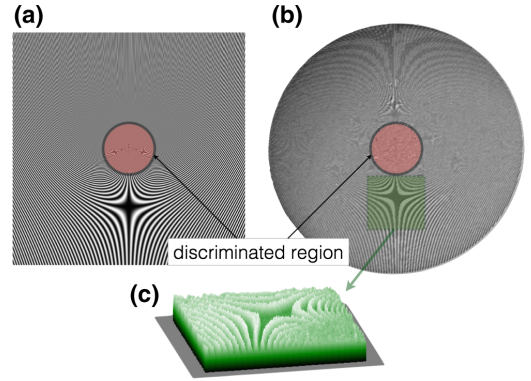


FIG. 1 (color online). (a) Designed CGH for generating an EVB with 200 twists. This CGH imprints a specific phase delay between  $[-\pi, \pi]$  onto the impinging beam. (b) SEM image of the nanofabricated phase hologram shown in (a). The hologram forms a pitchfork shape with 200 dislocations at the center. Because of high oscillation of the optical phase around the origin, shown in pink circles, the carrier changes more rapidly in a specific region where the phase alteration goes beyond the spatial resolution. (c) Thickness map of the shaded region of the fabricated hologram (see Supplemental Material for more details [25]).

to mill a silicon-nitride membrane. The thickness map of the fabricated hologram measured by energy loss mapping is shown in Fig. 1(c). The thickness of the hologram varies in the range of 120–180 nm, and the modulation depth is  $t_0 = 30$  nm. This provides enough phase change to tailor the phase of the electron wave packet, while for such large thickness the modulation in absorption is negligible.

As can be seen in Fig. 1, there exists a region [shown in pink circles in Figs. 1(a) and 1(b)] where the phase alteration is almost undefined, due to the presence of a phase singularity. This *dead region* can be blocked by an obstacle, as was proposed originally in Ref. [6], because the portion of the beam which passes through it is not affected by the mask. Nevertheless, as will be shown later, it affects the beam quality. Thus, we decided to compare and analyze the OAM spectrum of the generated beam for two different cases: when this dead central region is kept, and the case where the central region is obstructed.

We illuminated the hologram with a Schottky field emitter generated beam (a relatively coherent EB), in a JEOL 2200Fx transmission electron microscope with a convergence angle below  $0.3 \mu\text{rad}$  and a central energy of  $\mathcal{E} = 200$  keV. This corresponded to a de Broglie wavelength of  $\lambda = 2.5$  pm. The hologram [Fig. 1(b)] is inserted in the specimen position of the electron microscope. The EVB is generated in the low-magnification Lorentz mode as explained in Ref. [12]. The distribution of the electrons at the Fraunhofer plane is recorded, which provides a maximum separation between all orders of diffractions. Figure 2(a) shows the distribution of the electrons for first orders of diffraction, where the central

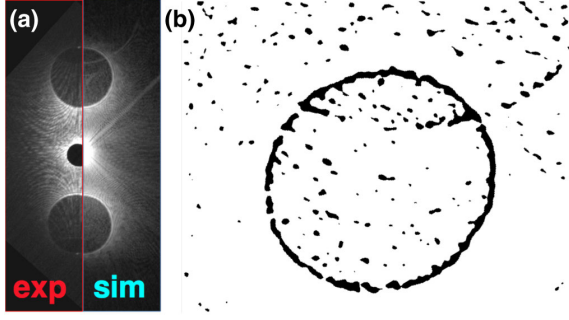


FIG. 2 (color online). (a) Experimentally (exp) observed and simulated (sim) Fraunhofer diffraction of a conventional EB from the CGH of Fig. 1(b). The upper and lower bright doughnuts are the  $\pm 1$  orders of diffraction. In order to increase the visibility of the first order of diffraction, the central beam is blocked by a beam stop. The hologram is symmetric, and thus both first orders of diffraction possess the same OAM value, nonetheless having an opposite sign. The distribution of the electrons that possess a phase singularity at the upper side (a) is calculated and shown in (b). The singularity tends to concentrate in a ring at the periphery of the dark region. This is achieved by measuring phase variation about an infinitesimal region close to each pixel at the upper diffraction area. As can be seen, the residual of the second order of diffraction with an OAM value of  $400\hbar$  (upper doughnut) is partially superimposed with the beam of first order. This lies in the fact that the diffraction angle of the electrons leaving the hologram is smaller than the divergence angle of the EB. Similar results are achieved for the hologram that its central region, shown in Fig. 1, is blocked.

beam is blocked by a beam stop. The first order of diffraction is zoomed in and shown in the map of Fig. 2(b). The generated EB is not pure, since there is residual of the beam at the second order of diffraction with an OAM value of  $400\hbar$  that overlaps with the first-order beam. However, the generated beam at the first order of diffraction is a quasi-coherent superposition of OAM states peaked about  $200\hbar$  with a different width and shape for two different types of holograms discussed above. The generated EVB, at the first order, can then be spatially filtered by means of an aperture. It is noteworthy to mention that the largest value of electron OAM ever reported [6] is created at the fourth order of diffraction with a very low efficiency. Conversely, in our case the generated beam is positioned at the first order of diffraction, which thanks to efficiency of the PM is much more intense ( $\gtrsim 30$  times brighter).

As the next step, the quality of generated highly twisted EBs for these two different holograms is analyzed. Indeed, we measure the phase front of the generated beam by performing the Fourier transform of the electron wave function at the exit facet of the hologram (see Supplemental Material for more details [25]). In order to do this, the thickness map of the hologram is obtained from the ratio between the elastic image and unfiltered image (see Ref. [12] for more details) and thus yields  $t(x, y)$ . This thickness  $t(x, y)$  is directly related to phase modulation  $\Delta\chi(x, y)$

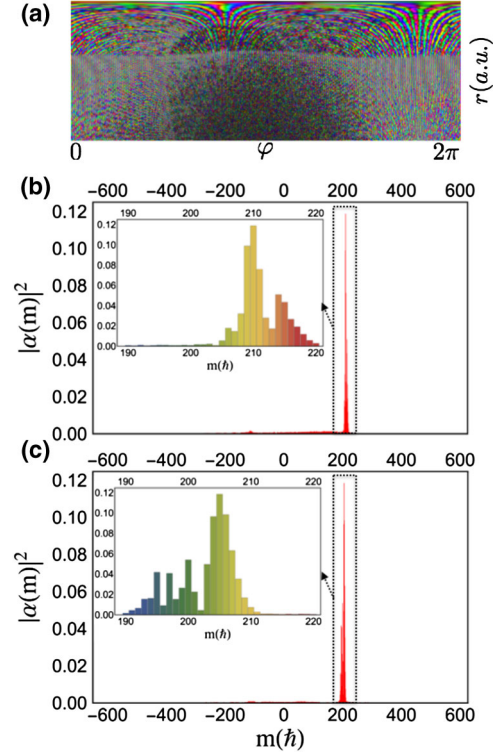


FIG. 3 (color online). (a) Calculated phase distribution of the electron wave function around the first order of diffraction. This is calculated by Fourier transforming the experimentally determined transfer function of the hologram from a *measured map* of the hologram thickness [see Fig. 1(c)]. The phase distribution is shown in polar coordinates, where the phase value is represented in a hue color. The OAM spectrum of the generated beam at the first order of diffraction from the hologram with and without the central *dead* region are shown in (b) and (c), respectively. This is measured by performing a one-dimensional Fourier transform of the azimuth coordinate. Because of imperfections at the origin and low spatial frequency for the case of (b), the beam is not pure and the value of OAM is delocalized centered around an OAM of  $(210.95 \pm 0.030)\hbar$ , while for the hologram with the excluded central dead region (c) the OAM spectrum central peak is about  $(202.75 \pm 0.032)\hbar$ . Indeed, the OAM spectrum, for both cases, moves to higher values mainly due to a small contribution from the second order of diffraction which carries an OAM of  $400\hbar$  [see Fig. 2(b)]. Nevertheless, the hologram with the excluded central dead region (c) gives much better results.

introduced by the hologram; see Eq. (1). This was verified by simulating the beam diffraction from such a PM. As is shown in Fig. 2(a), the simulation is in excellent agreement with the observed diffraction pattern and that of the hologram with the excluded dead region at the origin. The OAM spectrum is evaluated by transforming the electron wave function into polar coordinates and performing the Fourier transform in the azimuth coordinate. Figure 3(a) shows the unraveled phase of the electron in hue color, in polar coordinates. Thus, as expected by inspection of the shape of the diffracted beams, in both cases the OAM spectrum of the generated beam at the first order of diffraction is

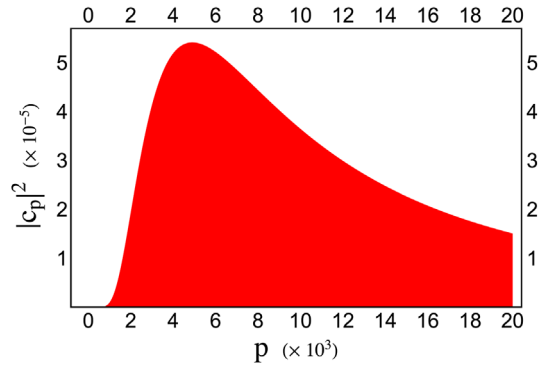


FIG. 4 (color online). Radial index distribution of the generated highly twisted EB with  $m = 200$  from the pitchfork hologram shown in Fig. 1. For simplicity, we assumed a hologram with *unlimited resolution*, and the size of hologram is reasonably larger than that of the impinging beam. The generated beam is delocalized in  $p$  space and has a peak around  $p = 4900$ .

delocalized. It is worth noticing that the generated beam is not simply a superposition of the two OAM values  $200\hbar$  and  $400\hbar$ , since these beams have different propagation axes. The OAM spectra for both holograms are shown in Figs. 3(b) and 3(c), respectively. The peak of OAM values is located around, but not exactly at,  $200\hbar$ . The reason lies in the fact that the high spatial frequencies can be mainly found in the missing details at the center of the hologram. This means that the intensity of the beam, due to overlapping with the residual of the second order of diffraction, is no longer azimuthally uniform as is expected for a beam that is an eigenstate of OAM.

This can be explained by the decomposition of the large vortex in many isolated first-order singularities. To demonstrate this, we need to characterize the position of the singularities. The topological charge  $m$  about a circle  $c$  is defined by  $m = 1/(2\pi) \oint_c \nabla\Phi \cdot d\ell$ , which gives the variation of phase around a path surrounding the origin. Using this definition, we construct many infinitesimal *steps* and map the position of the singularities. The resulting map is shown in Fig. 2(b). However, in our analysis the contribution of the zeroth order is excluded, since an annular postselection can remove its contribution. Finally, it is worth mentioning that the radial-index  $p$  distribution of the EVBs generated by such a PM is different from those of the Laguerre-Gaussian (LG) modes. EBs with LG mode distribution have a well-defined radial index  $p$  and are shape invariant upon free-space propagation. This is particularly important, since the evolution of EVBs in the presence of a longitudinal magnetic field  $B$  forms nondiffracting LG beams, so-called Landau states [19]. It has been shown that the transverse energy  $\mathcal{E}_\perp$  of these beams can be quantized according to Landau levels [26], given by  $\mathcal{E}_\perp = \hbar\Omega(2p + m + |m| + 1)$ , where  $\Omega = eB/(2m_e)$  is the Larmor frequency corresponding to the  $g$  factor of 1. The quantized transverse energy of the

electron depends on the radial index of the beam. The radial distribution of the EB at a given propagation distance  $z$  from the PM is given by  $f(r, z) \exp(im\varphi)$ , with

$$f(r, z) \propto \frac{e^{-(i\pi/z\lambda)r^2}}{z\lambda} \int_{r_{\min}}^{r_{\max}} J_m\left(\frac{2\pi r r'}{z\lambda}\right) \times e^{-[1+(i\pi w_0^2/z\lambda)](r'/w_0)^2} r' dr', \quad (2)$$

where  $J_m(x)$  is the Bessel function of integer order  $n$  and  $w_0$  is the beam radius at the PM, respectively.  $r_{\min}$  and  $r_{\max}$  are given by the active region of the hologram. For instance, for a relatively wide hologram of the first kind (the hologram with the central dead region),  $r_{\min} = 0$  and  $r_{\max} \rightarrow \infty$ . Thus, the emerging beam from the hologram is given in terms of hypergeometric-Gauss beams [27] (see Supplemental Material for more details [25]). Figure 4 shows the radial-index distribution of the generated beam from an  $m = 200$  pitchfork hologram. For the hologram with a truncated central region, the radial distribution of the electron is more complicated and should be calculated by Eq. (2). Therefore, the generated EB is a superposition of different LG modes having an azimuthal winding index  $m$  and radial index  $p$  distributions shown in Figs. 3 and 4, respectively. These imply a nonmonochromatic transverse energy distribution due to the indetermination of both, in the OAM and radial quantum indices.

In summary, we generated a highly twisted EB with an OAM quanta of  $200\hbar$ . This beam is generated by a holographic approach in which a nanofabricated pure phase hologram is used to manipulate a conventional beam into a form of EVB. The spectrum of OAM is calculated by measuring the thickness of the hologram and elaborating the diffraction pattern. Our analysis reveals that due to limited details on the PM, especially close to the origin, the generated beam contains a distribution of OAM. We believe that holographic generation of a *high- $m$*  vortex beam can potentially be an interesting method to explore the transition between the quantum and classical regimes of electromagnetic radiations inside a medium. Thus, it may be used to exploit the magnetic property of materials such as magnetic dichroism.

E. K. and R. W. B. acknowledge the support of the Canada Excellence Research Chairs (CERC) Program.

\*ekarimi@uottawa.ca

- [1] E. Rutherford, *Philos. Mag.* **21**, 669 (1911).
- [2] N. Bohr, *Philos. Mag.* **26**, 1 (1913).
- [3] K. Y. Bliokh, Y. P. Bliokh, S. Savel'ev, and F. Nori, *Phys. Rev. Lett.* **99**, 190404 (2007).
- [4] M. Uchida and A. Tonomura, *Nature (London)* **464**, 737 (2010).
- [5] J. Verbeeck, H. Tian, and P. Schattschneider, *Nature (London)* **467**, 301 (2010).

- [6] B. J. McMorran, A. Agrawal, I. M. Anderson, A. A. Herzing, H. J. Lezec, J. J. McClelland, and J. Unguris, *Science* **331**, 192 (2011).
- [7] J. Rusz, S. Bhowmick, M. Eriksson, and N. Karlsson, *Phys. Rev. B* **89**, 134428 (2014).
- [8] J. Verbeeck, G. Guzzinati, L. Clark, R. Juchtmans, R. V. Boxem, H. Tian, A. Béch e, A. Lubk, and G. Van Tendeloo, *C.R. Phys.* **15**, 190 (2014).
- [9] S. Lloyd, M. Babiker, and J. Yuan, *Phys. Rev. A* **88**, 031802 (2013).
- [10] S. Lloyd, M. Babiker, and J. Yuan, *Phys. Rev. Lett.* **108**, 074802 (2012).
- [11] J. Verbeeck, H. Tian, and G. Van Tendeloo, *Adv. Mater.* **25**, 1114 (2013).
- [12] V. Grillo, G. C. Gazzadi, E. Karimi, E. Mafakheri, R. W. Boyd, and S. Frabboni, *Appl. Phys. Lett.* **104**, 043109 (2014).
- [13] P. Schattschneider, M. St oger-Pollach, and J. Verbeeck, *Phys. Rev. Lett.* **109**, 084801 (2012).
- [14] E. Karimi, L. Marrucci, V. Grillo, and E. Santamato, *Phys. Rev. Lett.* **108**, 044801 (2012).
- [15] E. Karimi, V. Grillo, R. W. Boyd, and E. Santamato, *Ultramicroscopy* **138**, 22 (2014).
- [16] T. Petersen, M. Weyland, D. Paganin, T. Simula, S. Eastwood, and M. Morgan, *Phys. Rev. Lett.* **110**, 033901 (2013).
- [17] L. Clark, A. B ech e, G. Guzzinati, A. Lubk, M. Mazilu, R. Van Boxem, and J. Verbeeck, *Phys. Rev. Lett.* **111**, 064801 (2013).
- [18] I. P. Ivanov and D. V. Karlovets, *Phys. Rev. A* **88**, 043840 (2013).
- [19] K. Y. Bliokh, P. Schattschneider, J. Verbeeck, and F. Nori, *Phys. Rev. X* **2**, 041011 (2012).
- [20] N. Voloch-Bloch, Y. Lereah, Y. Lilach, A. Gover, and A. Arie, *Nature (London)* **494**, 331 (2013).
- [21] V. Grillo, E. Karimi, G. C. Gazzadi, S. Frabboni, M. R. Dennis, and R. W. Boyd, *Phys. Rev. X* **4**, 011013 (2014).
- [22] T. R. Harvey, J. S. Pierce, A. K. Agrawal, P. Ercius, M. Linck, and B. J. McMorran, *New J. Phys.* **16**, 093039 (2014).
- [23] L. Reimer and H. Kohl, *Transmission Electron Microscopy: Physics of Image Formation*, Vol. 36 (Springer, New York, 2008).
- [24] E. M uller, P. Kruse, D. Gerthsen, M. Schowalter, A. Rosenauer, D. Lamoen, R. Kling, and A. Waag, *Appl. Phys. Lett.* **86**, 154108 (2005).
- [25] See Supplemental Material at <http://link.aps.org/supplemental/10.1103/PhysRevLett.114.034801> which includes Refs. [12,26–28], for fabrication details, and mode analysis.
- [26] P. Schattschneider, T. Schachinger, M. St oger-Pollach, S. L offler, A. Steiger-Thirsfeld, K. Bliokh, and F. Nori, *Nat. Commun.* **5**, 4586 (2014).
- [27] E. Karimi, G. Zito, B. Piccirillo, L. Marrucci, and E. Santamato, *Opt. Lett.* **32**, 3053 (2007).
- [28] A. Lubk, G. Guzzinati, F. B orrnert, and J. Verbeeck, *Phys. Rev. Lett.* **111**, 173902 (2013).